A Perturbation Method for B_0 Field Calculations of Non-Conductive Objects

FMRIB Technical Report TR04MJ1
(A related paper is published in Magnetic Resonance in Medicine)

Mark Jenkinson, James Wilson and Peter Jezzard

Oxford Centre for Functional Magnetic Resonance Imaging of the Brain (FMRIB),
Department of Clinical Neurology, University of Oxford, John Radcliffe Hospital,
Headley Way, Headington, Oxford, UK

Abstract

Inhomogeneous B_0 fields produce artifacts in MR images including signal dropout and spatial distortion. We present a perturbative method for calculating the B_0 field to first order (error is second order). The perturbation parameter is the susceptibility difference between brain tissue and air: around 10 ppm. This method is advantageous as it is sufficiently accurate for most purposes, can be implemented as a simple convolution with a volumetric matter model, and is linear. Furthermore, the method is simple to use and can quickly calculate the field for any orientation of an object using a set of precalculated basis images.

1 Introduction

Theoretically calculating the B_0 field, given a matter distribution, allows modelling of MRI signal dropout, interaction of B_0 and motion effects, manipulation of B_0 using active and weakly magnetic passive shims, respiration effects, etc. Existing methods for calculating B_0 use full finite element calculations [1, 2] or approximate solutions to Maxwell's equations given either surface models of matter interfaces [3, 4], voxel-based elements [5] or Fourier representations [6]. By using a perturbation approach to solving Maxwell's equations [7], a linear first-order solution can be found which is fast and appropriate for most MR imaging applications. In addition, the perturbation method allows the magnitude of the errors to be calculated, and hence the accuracy and appropriateness of the method to be estimated for various applications.

2 Theory

Assuming the object is non-conductive (so $J = 0$), the relevant Maxwell's equations are

$$\nabla \times H = 0 \quad (1)$$

$$\nabla \cdot B = 0 \quad (2)$$

where $B = \mu H$, and the permeability, μ, is related to the susceptibility, χ, by

$$\mu = \mu_0(1 + \chi) \quad (3)$$

where μ_0 is the permeability of free-space.
These equations can be reduced to a single equation by using the magnetic scalar potential [8] $H = \nabla\phi$. This gives

$$\mu_0 \, \nabla \cdot (\, (1 + \chi)\nabla\phi) = 0. \quad (4)$$

Let the susceptibility, χ, be expanded as

$$\chi = \chi_0 + \delta\chi_1 \quad (5)$$

where χ_0 is the susceptibility of air (i.e. $\mu_{\mathrm{air}} = \mu_0(1+\chi_0)$ with $\chi_0 = 4\times10^{-7}$), and δ is a constant that represents the average difference in the susceptibility of brain tissue and air (e.g. -9.5×10^{-6} for brain tissues), such that the typical range of χ_1 is from 0 to 1.

Similarly, expand ϕ in a series

$$\phi = \phi_0 + \delta\phi_1 + \delta^2\phi_2 + \dots \tag{6}$$

This perturbation expansion in δ can be substituted back into equation 4 to give

$$\begin{aligned} \mu_0(1+\chi_0)\nabla^2\phi_0 &= 0 & (7)\\ (1+\chi_0)\nabla^2\phi_1 + \nabla\cdot(\chi_1\nabla\phi_0) &= 0 & (8)\end{aligned}$$

for the zeroth and first order terms in δ.
Using the zeroth order equation together with standard vector calculus identities gives a 3D Poisson equation

$$\nabla^2\phi_1 = \frac{-1}{1+\chi_0}\left(\nabla\cdot(\chi_1\nabla\phi_0)\right). \tag{9}$$

The Green's function for this equation is

$$G(\mathbf{x}) = \frac{-1}{4\pi r} \tag{10}$$

where $\mathbf{x} = (x, y, z)$ and $r = \|\mathbf{x}\| = \sqrt{x^2+y^2+z^2}$. This allows the solution of the Poisson equation to be written as a convolution

$$\phi_1(\mathbf{x}) = \iiint G(\mathbf{x}-\mathbf{x}')f(\mathbf{x}')\,d\mathbf{x}' \tag{11}$$

or more concisely as, $\phi_1 = G * f$, where $f = \frac{-1}{1+\chi_0}\left(\nabla\cdot(\chi_1\nabla\phi_0)\right)$.
From this the z-component of the B field can be written as

$$\begin{aligned} B_z &= \mu H_z = \mu\frac{\partial\phi}{\partial z} & (12)\\ &= \mu_0(1+\chi_0)\frac{\partial\phi_0}{\partial z} + \delta\,\mu_0\left(\chi_1\frac{\partial\phi_0}{\partial z} + (1+\chi_0)\frac{\partial\phi_1}{\partial z}\right) + O(\delta^2).\end{aligned}$$

As the zeroth order term is $B_z^{(0)} = \mu_0(1+\chi_0)\,\partial\phi_0/\partial z$, then the first order term is

$$B_z^{(1)} = \frac{\chi_1}{1+\chi_0}B_z^{(0)} + \mu_0(1+\chi_0)\frac{\partial\phi_1}{\partial z}. \tag{13}$$

Using the fact that

$$\frac{\partial}{\partial x}(G*f) = G*\frac{\partial f}{\partial x} = \frac{\partial G}{\partial x}*f$$

holds for any G and f, together with equations 7, 8, 11 and 13, gives

$$B_z^{(1)} = \frac{\chi_1}{1+\chi_0}B_z^{(0)} - \frac{1}{1+\chi_0}\left(\left(\frac{\partial^2 G}{\partial x\partial z}\right)*\left(\chi_1 B_x^{(0)}\right) + \left(\frac{\partial^2 G}{\partial y\partial z}\right)*\left(\chi_1 B_y^{(0)}\right) + \left(\frac{\partial^2 G}{\partial z^2}\right)*\left(\chi_1 B_z^{(0)}\right)\right) \tag{14}$$

2.1 Lorentz Correction

The solution derived above is valid for continuous media. However, to know the field applied to the ^{1}H nuclei in MR, it is necessary to take account of the discrete nature of the media. The desired field is that applied externally to the nuclei, and can be calculated from the continuous field using the Lorentz Correction [9, 8]. The corrected field is given by

$$B_{LC} = B - \frac{2}{3}\mu_0 M = B - \frac{2}{3}\left(\frac{\chi}{1+\chi}\right)B = \left(\frac{3+\chi}{3+3\chi}\right)B \tag{15}$$

where $M = \chi H$ is the magnetization of the material. Hence the zeroth and first order corrections can be calculated from the expansion of

$$\begin{aligned} B_{LC}^{(0)} + \delta B_{LC}^{(1)} &= \left(\frac{3+\chi_0}{3+3\chi_0} - \delta\frac{2\chi_1}{3(1+\chi_0)^2}\right)\left(B^{(0)} + \delta B^{(1)}\right) + O(\delta^2) & (16)\\ &= \frac{3+\chi_0}{3+3\chi_0}B^{(0)} + \delta\left(\frac{3+\chi_0}{3+3\chi_0}B^{(1)} - \frac{2\chi_1}{3(1+\chi_0)^2}B^{(0)}\right) + O(\delta^2) & (17)\end{aligned}$$

Consequently, the corrected field solution becomes

$$B^{(1)}_{LC,z} = \frac{\chi_1}{3+\chi_0} B^{(0)}_{LC,z} - \frac{1}{1+\chi_0}\left(\left(\frac{\partial^2 G}{\partial x \partial z}\right) * \left(\chi_1 B^{(0)}_{LC,x}\right) + \left(\frac{\partial^2 G}{\partial y \partial z}\right) * \left(\chi_1 B^{(0)}_{LC,y}\right) + \left(\frac{\partial^2 G}{\partial z^2}\right) * \left(\chi_1 B^{(0)}_{LC,z}\right)\right). \quad (18)$$

For the rest of this paper, only the Lorentz Corrected fields will be used although the LC subscript will be dropped. Note that the zeroth order fields are also Lorentz Corrected, which is appropriate if they are calibrated from NMR frequency results, since the frequency is determined by the corrected field strength.

2.2 Single Voxel Solution

Equation 14 allows the first order $B^{(1)}_z$ field to be calculated if the zeroth order field $B^{(0)}$ and the susceptibility distribution χ_1 are known. The zeroth order field represents the field which would be present if there were no object in the scanner (e.g. constant field in the z direction).
The susceptibility distribution represents the object in the scanner and needs to be specified at each point in space. For complicated functions though, the required convolutions are difficult, if not impossible, to do analytically. For most purposes, however, it is sufficient to approximate the object using small rectangular volume elements (voxels). The advantage of this is that the convolution can be done analytically for a single voxel.
Consider a single voxel of dimensions (a, b, c), and without loss of generality, let it be centred at the origin $(0, 0, 0)$ with a susceptibility of $\chi_1 = 1$ within the voxel and $\chi_1 = 0$ outside the voxel. Given this, the required convolutions in equation 14 can be written as

$$\begin{aligned}\left(\frac{\partial^2 G}{\partial v \partial z}\right) * \left(\chi_1 B^{(0)}_v\right) &= \iiint \chi_1(\mathbf{x}-\mathbf{x}') B^{(0)}_v(\mathbf{x}-\mathbf{x}') \frac{\partial^2 G}{\partial v \partial z}(\mathbf{x}')\, d\mathbf{x}' \\ &= \int_{x-a/2}^{x+a/2} dx' \int_{y-b/2}^{y+b/2} dy' \int_{z-c/2}^{z+c/2} dz' \, \frac{\partial^2 G}{\partial v \partial z}(\mathbf{x}') B^{(0)}_v(\mathbf{x}-\mathbf{x}'). \end{aligned} \quad (19)$$

where v stands for either x, y or z.
The last integral can be easily calculated from the indefinite integral, which we will denote here as $F(\mathbf{x}'; \mathbf{x})$. That is

$$F(\mathbf{x}'; \mathbf{x}) = F(x', y', z'; \mathbf{x}) = \iiint \frac{\partial^2 G}{\partial v \partial z}(\mathbf{x}') B^{(0)}_v(\mathbf{x}-\mathbf{x}')\, dx'\, dy'\, dz'. \quad (20)$$

giving the single voxel solution as

$$\begin{aligned} H_{v,z}(\mathbf{x}) = \left(\frac{\partial^2 G}{\partial v \partial z}\right) * \left(\chi_1 B^{(0)}_v\right) = \quad & F(x+a/2, y+b/2, z+c/2; \mathbf{x}) - F(x-a/2, y+b/2, z+c/2; \mathbf{x}) \\ & -F(x+a/2, y-b/2, z+c/2; \mathbf{x}) - F(x+a/2, y+b/2, z-c/2; \mathbf{x}) \\ & +F(x-a/2, y-b/2, z+c/2; \mathbf{x}) + F(x-a/2, y+b/2, z-c/2; \mathbf{x}) \\ & +F(x+a/2, y-b/2, z-c/2; \mathbf{x}) - F(x-a/2, y-b/2, z-c/2; \mathbf{x}). \end{aligned} \quad (21)$$

2.2.1 Constant Fields

Case 1: $B^{(0)}(\mathbf{x}) = (0, 0, 1)$

Using $G(\mathbf{x}') = \frac{-1}{4\pi r'}$ where $r' = \|\mathbf{x}'\|$ gives

$$\begin{aligned} F(\mathbf{x}'; \mathbf{x}) &= \iiint \frac{\partial^2 G}{\partial z'^2}\, dx'\, dy'\, dz' \\ &= \iint \frac{\partial G}{\partial z'}\, dx'\, dy' \\ &= \iint \frac{z'}{4\pi r'^3}\, dx'\, dy' \\ &= \frac{1}{4\pi} \operatorname{atan}\left(\frac{x'y'}{z'r'}\right) \end{aligned} \quad (22)$$

where equation 30 from the Appendix was used in the last step.
By substituting this into equations 14 and 21, the field $B^{(1)}_z$ can be calculated for this case. Note that provided the z axis corresponds to the main static (constant) B_0 field, then this case is all that is required for the field calculation of a non-conducting object.

Case 2: $B^{(0)}(\mathbf{x}) = (1, 0, 0)$

$$\begin{aligned} F(\mathbf{x}';\mathbf{x}) &= \iiint \frac{\partial^2 G}{\partial x' \partial z'}\, dx'\, dy'\, dz' \\ &= \int G\, dy' \\ &= \frac{-1}{4\pi} \sinh^{-1}\left(\frac{y'}{\sqrt{x'^2 + z'^2}}\right) \end{aligned} \tag{23}$$

using equation 29 from Appendix A.
Again, this can be substituted into equations 14 and 21 to get $B_z^{(1)}$.

Case 3: $B^{(0)}(\mathbf{x}) = (0, 1, 0)$

This is the same as the previous case except all x's and y's are swapped.

Note that the single voxel solution, $F(\mathbf{x}';\mathbf{x})$, in a constant field does not involve the *unprimed* coordinates, $\mathbf{x}$. Solutions when the zeroth order field involves a linear spatial gradient can be found in Appendix B and do involve both primed and unprimed coordinates.

2.3 Combining Voxels

Due to the linearity of equation 18 the single voxel solutions derived in the previous section can be added together to give the total field for the object as

$$B_z^{(1)}(\mathbf{x}) = \sum_{\mathbf{x}'} \chi_1(\mathbf{x}') H(\mathbf{x} - \mathbf{x}'). \tag{24}$$

This takes the form of a discrete convolution of the discrete susceptibility map, χ_1, and the single voxel solution, H. Therefore the calculation can be efficiently implemented by using the 3D Fast Fourier Transform (FFT) as

$$B_z = \mathcal{F}^{-1}\left(\mathcal{F}(Z(\chi_1))\mathcal{F}(H)\right) \tag{25}$$

where $\mathcal{F}(\cdots)$ is the FFT and $Z(\cdots)$ is a zero-padding function, used to ensure that there is no period wrap-around in the convolution.

2.4 Gradient of the Perturbed Field

The exact analytical gradient of the perturbed field $B^{(1)}$ can be calculated by simply replacing the convolution kernel, H, with its gradient and neglecting the first term, since it is proportional to $\chi_1 B^{(0)}$ and has zero gradient at the centre of the voxel. This can be also be seen from equation 24 which gives

$$\frac{\partial B^{(1)}}{\partial q} = \sum_{\mathbf{x}'} \chi_1(\mathbf{x}') \left.\frac{\partial H}{\partial q}\right|_{(\mathbf{x}-\mathbf{x}')} \tag{26}$$

where q stands for x, y or z.

2.5 Changing Orientation

Calculating the field produced by a rotated object is equivalent to calculating the field produced by rotated applied fields — that is, applying rotated $\mathbf{B}^{(0)}$. Note that the latter calculation is in the reference frame of the object, not the scanner, and so calculating the scanner defined z component of the perturbed field requires projection onto the scanner frame z axis unit vector. Furthermore, since $\mathbf{B}^{(1)}$ is a linear function of $\mathbf{B}^{(0)}$ then

rotating $\mathbf{B}^{(0)}$ is equivalent to rotating $\mathbf{B}^{(1)}$. Hence the scanner defined z component of the perturbed field resulting from an applied field $B^{(0)}$ in the z direction is

$$\widetilde{B}_z^{(1)} = [0\ 0\ 1]\, R^{-1} \begin{bmatrix} B_x^{(1)}(1,0,0) & B_x^{(1)}(0,1,0) & B_x^{(1)}(0,0,1) \\ B_y^{(1)}(1,0,0) & B_y^{(1)}(0,1,0) & B_y^{(1)}(0,0,1) \\ B_z^{(1)}(1,0,0) & B_z^{(1)}(0,1,0) & B_z^{(1)}(0,0,1) \end{bmatrix} R \begin{bmatrix} 0 \\ 0 \\ 1 \end{bmatrix} \tag{27}$$

where R is a 3×3 matrix that represents the rotation from the scanner to the object coordinate system, that is $\mathbf{x_{ob}} = R\mathbf{x_{sc}}$, and $B_p^{(1)}(\hat{\mathbf{q}})$ is the field calculated in the p direction (x, y or z) from an applied field $B^{(0)} = \hat{\mathbf{q}}$ (being either $\hat{\mathbf{x}}, \hat{\mathbf{y}}$ or $\hat{\mathbf{z}}$).

In practice, the matrix of perturb fields, $[B_p^{(1)}(\hat{\mathbf{q}})]$, acts as a set of 9 basis images, which can be precalculated and then combined as specified to give the desired field at any orientation. This does not involve further approximation, it is precisely the same perturbed field that would be calculated for the object in the new orientation. In addition, although the perturbed field is linear in the basis images, it is not linear in the rotation angles, since the elements of R are non-linear functions of these angles.

A similar calculation can be done for the gradients of the field, $\nabla B^{(1)}$.

3 Validation and Results

3.1 Analytical Sphere

The analytical magnetic field (including Lorentz Correction) produced by a spherical object of radius R_0 and susceptibility χ_i inside a medium of susceptibility χ_e is given by

$$B_z = \begin{cases} B_0 + \frac{\chi_i - \chi_e}{3+\chi_e}(\frac{R_0}{r})^3(3\cos^2\theta - 1)B_0 & \text{for} \quad r > R_0 \\ B_0 & \text{for} \quad r < R_0 \end{cases} \tag{28}$$

where cylindrical coordinates are used with θ being the angle to the positive z axis.

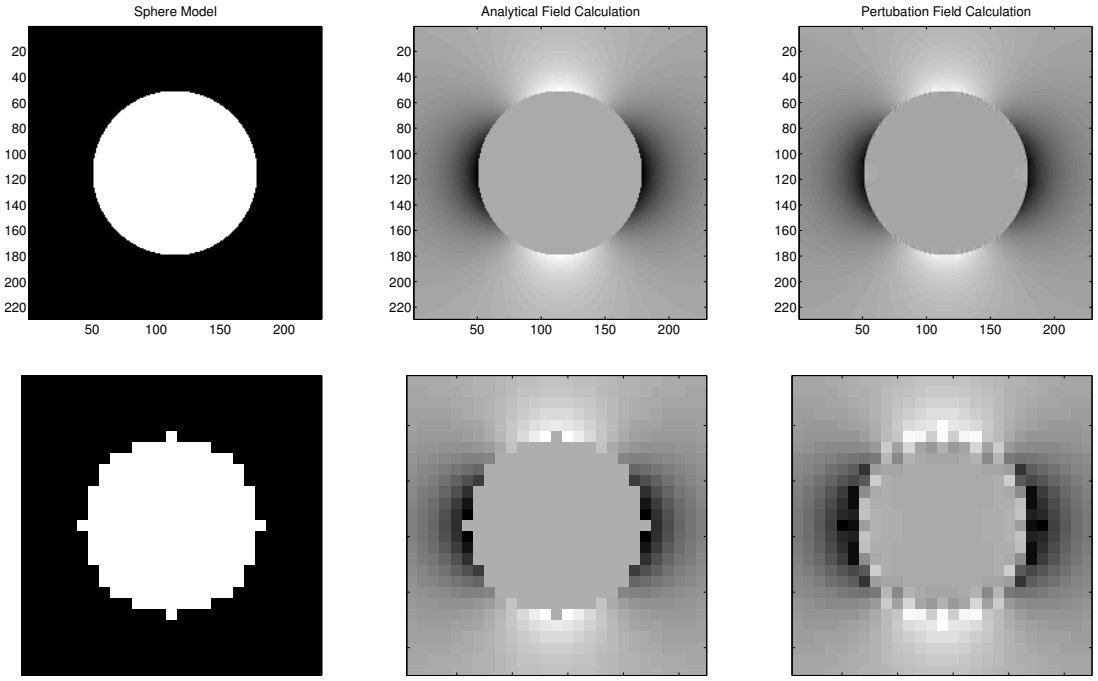

Figure 1: Sphere object model (left), analytical field (middle) and perturbation field calculation (right) for two sizes of sphere: $R_0 = 64$ (top row) and $R_0 = 8$ (bottom row).

Figure 1 show the field distribution (less B_0) along the z axis of a sphere, comparing the analytical solution given in equation 28 with the solution calculated with the perturbation method. Figure 2 shows plots through

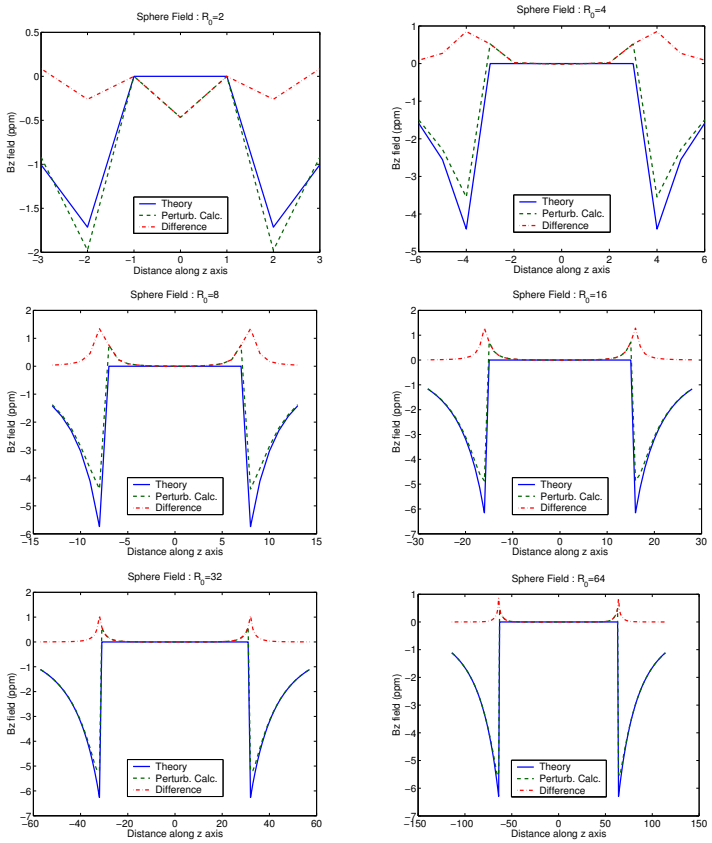

Figure 2: Plots of the B_z distribution along the z axis for spherical objects of radius $R_0 = 2, 4, 8, 16, 32, 64$ voxels. Results are shown for the analytical calculation (theory), the perturbation calculation and the difference between the two. Note that the values are only calculated at the centres of the voxels — hence the noticeably non-vertical sides in the $R_0 = 2$ case.

the centres of these spheres for a range of different radii, $R_0 = 2, 4, 8, 16, 32, 64$ mm, where in each case the voxel size is $1 \times 1 \times 1$ mm. This demonstrates the relationship between spatial extent and size of the error, where it can be seen that the maximum error is approximately equal to 1 ppm in all cases, with the spatial extent of significant errors covering 5 voxels or so. These results are very similar to those shown in [4, 1, 2, 5] despite the range of different object models (e.g. boundary element methods vs voxels) and approximations used.

3.2 *In-vivo* Human Head

An experimentally acquired field map of an *in-vivo* human head was used to validate the method in practice. The MR field map sequence used a symmetric-asymmetric spin-echo pair [10, 11] (2.5ms asymmetry time; $128 \times 256 \times 20$ voxels of size $1.5 \times 1.0 \times 6.0mm$). The theoretical field map was calculated using an object susceptibility map that was created from a $112 \times 164 \times 156$ ($1.0 \times 1.0 \times 1.0mm$), segmented CT image (as it discriminates between bone and air), which was registered to the MR image corresponding to the acquired field map.
Figure 3 shows slices from the CT image used to define the object susceptibility map, plus both the experimentally acquired field map and the field map calculated using the voxel-based perturbation method described above (execution time was 9 minutes on a 1.8GHz Athlon, 2GB memory running Linux). Note that both field maps have been masked so that only brain tissue is included (although the simulation included all tissues present, with $\chi_{\text{brain}} = \chi_{\text{bone}} = 1.0$) and have had the first and second-order spherical harmonics removed in order to factor out the effect of the shims on the field maps.
Qualitatively it can be seen that the match is good. Quantitatively the mean absolute difference between the field maps is 0.05 ppm, while the typical range of the field values (used for the display range in Fig. 3) is $\pm 0.4ppm$. The calculated error can also be compared with the neglected second order terms in the perturbation expansion. These second order terms have an approximate magnitude of $\delta^2 = 10^{-10} = 0.0001ppm$, which is two orders of magnitude less than the observed errors. However, there is also another error contribution, from the the inaccuracies in modelling the object as a set of rectangular voxels, which is dominant in this case.

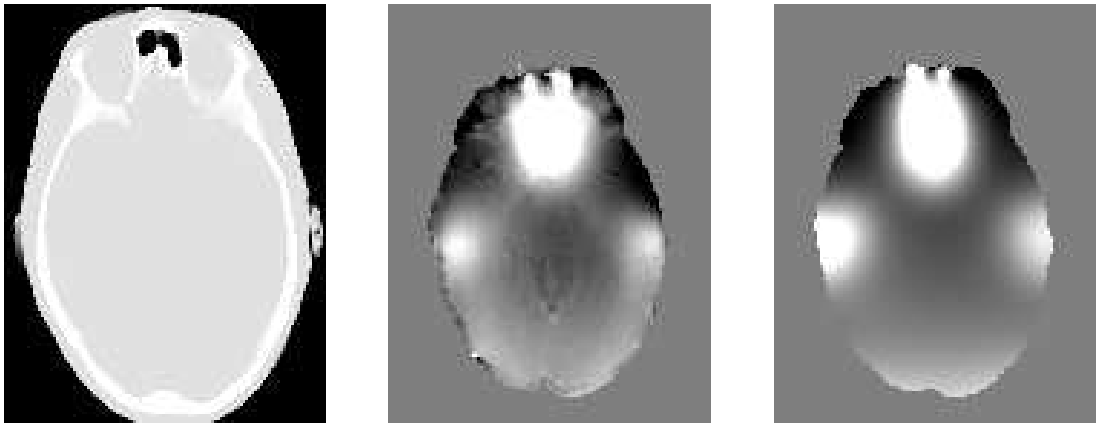

Figure 3: Corresponding slices from images of an *in-vivo* human head, showing the CT image used to derive the susceptibility map (left), the experimentally acquired field map (middle) and the field map from the voxel-based perturbation calculation (right). The displayed scale of the field maps is ± 0.4 ppm.

4 Discussion

In this paper we present a perturbation method for calculating the B_0field for an object with varying spatial susceptibility. A fast, first-order calculation is presented for voxel-based objects, using the analytical voxel solution. The accuracy of this method is tested using the analytical solution for a sphere as well as phantom and human *in-vivo* data. These results indicate that highly localised errors of less than 1 ppm are achieved generally, which is very similar to other calculation methods, and sufficient for most MR imaging purposes.
There are several main contributions from this work. The first is the use of a principled, perturbation method for arriving at the field approximation. This is useful in that it allows the magnitude of the error terms (second-order and higher) to be estimated which then permits the relevant applicability of the method to be assessed.

For instance, the method cannot be used for metallic objects where the susceptibility difference, δ, is large, but can be used for some slightly higher susceptibility substances like graphite [11]. Without knowledge of how these errors scale it is not possible to know when to have confidence in applying an approximation without substantial experimental testing and validation. It is also possible, although potentially analytically intractable, to extend the approximation to higher orders to increase the accuracy. In addition, the formulation of the perturbation equations is separate from the object model specification and could be used with other object models, such as boundary element methods.

The other significant contribution of this work is the ability to calculate more than just the z component of the field. In particular, the x and y components can be calculated just as easily (although separately) as well as the gradients of the fields (evaluated at the voxel centres), and formulations are provided for all these cases. More interestingly, it is possible to calculate the field at different object orientations by linearly combining 'basis' images. This allows the field to be determined, without further approximation, at any orientation in a very efficient manner, if the basis images have been precalculated and stored. Such calculations will allow the interaction between susceptibility fields and motion artefacts to be explored more easily, a current research interest of the authors.

In the field calculations used here there are two main sources of approximation: (1) neglecting all terms beyond the first-order term and (2) representing the object by a voxel-based model. The first approximation limits the range of objects for which this method could be applied. For instance, it is not useful for metallic objects which have very large δ and potentially non-zero currents, but is applicable for the typical range of biological tissues encountered.

The second approximation is potentially more limiting, as the use of a voxel-based model for the object will cause errors that are not as easily estimated as the perturbation approximation errors. In particular, voxel-based models are likely to cause greater errors in the calculation for large voxel sizes, especially at the boundaries, as indicated in the sphere results (see Figure 2). By reducing the size of the voxels the spatial extent of this error can be reduced. Alternative models such as boundary element methods [4, 1, 3, 2] are likely to be physically accurate in capturing the object shape, but have two main disadvantages. One is that boundary meshes are more difficult to instantiate from images and the second is that they require more computation for the field calculation as each element (triangle of the mesh) is potentially unique and requires separate calculations. In contrast, voxel-based models [12, 5] are easy to instantiate and very efficient to calculate (using Fast Fourier Transforms). Furthermore, the numerical results on the spherical object indicate that similar errors are obtained, regardless of the method chosen. Finally, both of these object models have an advantage over finite Fourier representations [6] since they can ensure that the object has finite spatial extent, which is not possible with the Fourier method.

Appendices

A Integrals

The following integrals are required for calculating the necessary Green's functions of a single voxel. They are contained in [13]. Given $r = \sqrt{x^2 + y^2 + z^2}$

$$\int \frac{1}{r}\,dy = \sinh^{-1}\left(\frac{y}{\sqrt{x^2+z^2}}\right) \tag{29}$$

$$\iint \frac{1}{r^3}\,dx\,dy = \frac{1}{z}\operatorname{atan}\left(\frac{xy}{zr}\right) \tag{30}$$

$$\iint \frac{1}{r}\,dx\,dy = y\sinh^{-1}\left(\frac{x}{\sqrt{y^2+z^2}}\right) + x\sinh^{-1}\left(\frac{y}{\sqrt{x^2+z^2}}\right) - z\operatorname{atan}\left(\frac{xy}{zr}\right) \tag{31}$$

B Applied Gradient Field Solutions

For gradient fields it is necessary to account for the Maxwell terms. That is, fields that exist in addition to the desired gradient of $B_z^{(0)}$ due to the fact that $\nabla^2\phi_0 = 0$. Once ϕ_0 is found, then $B^{(0)}$ is proportional to $\nabla\phi_0$.

For example, if an x-gradient in the z field is desired, $B_z^{(0)} = x$, then $\partial\phi_0/\partial z = x$ (up to a constant). Consequently, $\phi_0 = xz$, which already satisfies $\nabla^2\phi_0 = 0$. However, for $B_z^{(0)} = z$, then $\phi_0 = z^2/2$ cannot be used as

$\nabla^2\phi_0 = 1$. Consequently, $\phi_0 = z^2/2 - x^2/2$ (or some other equivalent using x and y in the second term) must be used instead.

Case 1: $B^{(0)}(\mathbf{x}) = (-x, 0, z)$

Now there are two terms to be calculated. Firstly,

$$\begin{aligned}
F_1(\mathbf{x}';\mathbf{x}) &= \iiint(-x+x')\frac{\partial^2 G}{\partial x'\partial z'}\,dx'\,dy'\,dz' \\
&= -\int xG\,dy' + \iint x'\frac{\partial G}{\partial x'}\,dx'\,dy' \\
&= -\int xG\,dy' + \int x'G\,dy' - \iint G\,dx'\,dy' \\
&= \frac{x-x'}{4\pi}\sinh^{-1}\left(\frac{y'}{\sqrt{x'^2+z'^2}}\right) \\
&\quad + \frac{1}{4\pi}\left(y'\sinh^{-1}\left(\frac{x'}{\sqrt{y'^2+z'^2}}\right) + x'\sinh^{-1}\left(\frac{y'}{\sqrt{x'^2+z'^2}}\right) - z'\operatorname{atan}\left(\frac{x'y'}{z'r'}\right)\right) \\
&= \frac{x}{4\pi}\sinh^{-1}\left(\frac{y'}{\sqrt{x'^2+z'^2}}\right) + \frac{y'}{4\pi}\sinh^{-1}\left(\frac{x'}{\sqrt{y'^2+z'^2}}\right) - \frac{z'}{4\pi}\operatorname{atan}\left(\frac{x'y'}{z'r'}\right) \qquad (32)
\end{aligned}$$

and secondly

$$\begin{aligned}
F_2(\mathbf{x}';\mathbf{x}) &= \iiint(z-z')\frac{\partial^2 G}{\partial z'^2}\,dx'\,dy'\,dz' \\
&= z\iiint\frac{\partial^2 G}{\partial z'^2}\,dx'\,dy'\,dz' - \iiint z'\frac{\partial^2 G}{\partial z'^2}\,dx'\,dy'\,dz' \\
&= \iint z\frac{\partial G}{\partial z'}\,dx'\,dy' - \iint z'\frac{\partial G}{\partial z'}\,dx'\,dy' + \iiint\frac{\partial G}{\partial z'}\,dx'\,dy'\,dz' \\
&= \frac{z}{4\pi}\operatorname{atan}\left(\frac{x'y'}{z'r'}\right) - \iint\frac{z'^2}{4\pi r'^3}\,dx'\,dy' + \iint G\,dx'\,dy' \\
&= \frac{z}{4\pi}\operatorname{atan}\left(\frac{x'y'}{z'r'}\right) - \frac{z'}{4\pi}\operatorname{atan}\left(\frac{x'y'}{z'r'}\right) \\
&\quad - \frac{1}{4\pi}\left(y'\sinh^{-1}\left(\frac{x'}{\sqrt{y'^2+z'^2}}\right) + x'\sinh^{-1}\left(\frac{y'}{\sqrt{x'^2+z'^2}}\right) - z'\operatorname{atan}\left(\frac{x'y'}{z'r'}\right)\right) \\
&= \frac{z}{4\pi}\operatorname{atan}\left(\frac{x'y'}{z'r'}\right) - \frac{y'}{4\pi}\sinh^{-1}\left(\frac{x'}{\sqrt{y'^2+z'^2}}\right) - \frac{x'}{4\pi}\sinh^{-1}\left(\frac{y'}{\sqrt{x'^2+z'^2}}\right) \qquad (33)
\end{aligned}$$

Due to the linearity of equations 14 and 21 these two terms can be combined at this stage to give

$$\begin{aligned}
F(\mathbf{x}';\mathbf{x}) &= F_1(\mathbf{x}';\mathbf{x}) + F_2(\mathbf{x}';\mathbf{x}) \\
&= \frac{x-x'}{4\pi}\sinh^{-1}\left(\frac{y'}{\sqrt{x'^2+z'^2}}\right) + \frac{z-z'}{4\pi}\operatorname{atan}\left(\frac{x'y'}{z'r'}\right) \qquad (34)
\end{aligned}$$

which can be substituted directly to give $B_z^{(1)}$.
Note that for F_1 and F_2 here both primed and *unprimed* coordinates appear, whereas for the constant fields the unprimed coordinates did not appear in the expressions for F.

Case 2: $B^{(0)}(\mathbf{x}) = (z, 0, x)$

Two terms need to be calculated. Firstly,

$$\begin{aligned}
F_1(\mathbf{x}';\mathbf{x}) &= \iiint (z-z')\frac{\partial^2 G}{\partial x' \partial z'}\,dx'\,dy'\,dz' \\
&= \int zG\,dy' - \iint z'\frac{\partial G}{\partial z'}\,dy'\,dz' \\
&= \int zG\,dy' - \int z'G\,dy' + \iint G\,dy'\,dz' \\
&= \frac{z'-z}{4\pi}\sinh^{-1}\left(\frac{y'}{\sqrt{x'^2+z'^2}}\right) - \frac{1}{4\pi}\iint \frac{1}{r'}\,dy'\,dz' \\
&= \frac{z'-z}{4\pi}\sinh^{-1}\left(\frac{y'}{\sqrt{x'^2+z'^2}}\right) \\
&\quad -\frac{1}{4\pi}\left(y'\sinh^{-1}\left(\frac{z'}{\sqrt{y'^2+x'^2}}\right) + z'\sinh^{-1}\left(\frac{y'}{\sqrt{x'^2+z'^2}}\right) - x'\operatorname{atan}\left(\frac{z'y'}{x'r'}\right)\right) \\
&= \frac{x'}{4\pi}\operatorname{atan}\left(\frac{z'y'}{x'r'}\right) - \frac{z}{4\pi}\sinh^{-1}\left(\frac{y'}{\sqrt{x'^2+z'^2}}\right) - \frac{y'}{4\pi}\sinh^{-1}\left(\frac{z'}{\sqrt{y'^2+x'^2}}\right)
\end{aligned} \tag{35}$$

and secondly

$$\begin{aligned}
F_2(\mathbf{x}';\mathbf{x}) &= \iiint (x-x')\frac{\partial^2 G}{\partial z'^2}\,dx'\,dy'\,dz' \\
&= \iint x\frac{\partial G}{\partial z'}\,dx'\,dy' - \iint x'\frac{\partial G}{\partial z'}\,dx'\,dy' \\
&= \frac{x}{4\pi}\operatorname{atan}\left(\frac{x'y'}{z'r'}\right) - \iint x'\frac{z'}{4\pi r'^3}\,dx'\,dy' \\
&= \frac{x}{4\pi}\operatorname{atan}\left(\frac{x'y'}{z'r'}\right) + \int \frac{z'}{4\pi r'}\,dy' \\
&= \frac{x}{4\pi}\operatorname{atan}\left(\frac{x'y'}{z'r'}\right) + \frac{z'}{4\pi}\sinh^{-1}\left(\frac{y'}{\sqrt{x'^2+z'^2}}\right).
\end{aligned} \tag{36}$$

Due to the linearity of equations 14 and 21 these two terms can be combined at this stage to give

$$\begin{aligned}
F(\mathbf{x}';\mathbf{x}) &= F_1(\mathbf{x}';\mathbf{x}) + F_2(\mathbf{x}';\mathbf{x}) \\
&= \frac{x}{4\pi}\operatorname{atan}\left(\frac{x'y'}{z'r'}\right) + \frac{x'}{4\pi}\operatorname{atan}\left(\frac{z'y'}{x'r'}\right) + \frac{z'-z}{4\pi}\sinh^{-1}\left(\frac{y'}{\sqrt{x'^2+z'^2}}\right) - \frac{y'}{4\pi}\sinh^{-1}\left(\frac{z'}{\sqrt{y'^2+x'^2}}\right)
\end{aligned}$$

which can be substituted directly to give $B_z^{(1)}$.
Once again, note that for F_1 and F_2 here both primed and *unprimed* coordinates appear, whereas for the constant fields the unprimed coordinates did not appear in the expressions for F.

Case 3: $B^{(0)}(\mathbf{x}) = (0, z, y)$

This is the same as the previous case except all x's and y's are swapped.

C Kernels for Gradient Field Calculations

To calculate the gradient of the perturbed fields at the voxel centres, the same calculation method used for the main field can be employed, but using the gradient of the kernels, ∇F, rather than F. In particular,

$$\frac{\partial F(\mathbf{x}';\mathbf{x})}{\partial q} = \frac{\partial F(\mathbf{x}';\mathbf{x})}{\partial \mathbf{x}'}\frac{\partial \mathbf{x}'}{\partial q} + \frac{\partial F(\mathbf{x}';\mathbf{x})}{\partial \mathbf{x}}\frac{\partial \mathbf{x}}{\partial q} \tag{37}$$

which reduces to

$$\frac{\partial F(\mathbf{x}';\mathbf{x})}{\partial q} = \frac{\partial F(\mathbf{x}';\mathbf{x})}{\partial q'} \tag{38}$$

when $F(\mathbf{x}';\mathbf{x}) = F(\mathbf{x}')$ and $q = x, y$ or z.

Case 1: $B^{(0)}(\mathbf{x}) = (0, 0, 1)$

$$\nabla F(\mathbf{x}'; \mathbf{x}) = \nabla \frac{1}{4\pi} \text{atan}\left(\frac{x'y'}{z'r'}\right) \tag{39}$$

$$= \frac{1}{4\pi}\left[\frac{y'z'}{x'^2 + z'^2}\ ,\ \frac{x'z'}{y'^2 + z'^2}\ ,\ \frac{-x'y'(r'^2 + z'^2)}{(x'^2 + z'^2)(y'^2 + z'^2)}\right] \tag{40}$$

Case 2: $B^{(0)}(\mathbf{x}) = (1, 0, 0)$

$$\nabla F(\mathbf{x}'; \mathbf{x}) = \nabla \frac{-1}{4\pi} \sinh^{-1}\left(\frac{y'}{\sqrt{x'^2 + z'^2}}\right) \tag{41}$$

$$= \frac{1}{4\pi}\left[\frac{x'y'}{r'(x'^2 + z'^2)}\ ,\ \frac{-1}{r'}\ ,\ \frac{y'z'}{r'(x'^2 + z'^2)}\right] \tag{42}$$

Similar calculations can be performed when the applied field includes a linear gradient by taking the kernels calculated in Appendix B.

Acknowledgements

We would like to thank Dr Bob Cox for suggesting that a perturbation calculation could be useful for magnetic field calculations in a conference presentation on motion artefacts. We also acknowledge support from the UK EPSRC (MIAS-IRC), GlaxoSmithKline and the UK Medical Research Council.

References

[1] S. Li, B. J. Dardzinski, C. M. Collins, Q. X. Yang, and M. B. Smith. Three-dimensional mapping of the static magnetic field inside the human head. *Magn Reson Med*, **36**, 705–714. (1996).

[2] C. M. Collins, B. Yang, Q. X. Yang, and M. B. Smith. Numerical calculations of the static magnetic field in three-dimensional multi-tissue models of the human head. *Magn Reson Imaging*, **20**, 413–424. (2002).

[3] S. Balac and G. Caloz. Magnetic susceptibility artifacts in magnetic resonance imaging: calculation of the magnetic field disturbances. *IEEE Trans Magnetics*, **32**, 1645–1648. (1996).

[4] J. D. de Munck, R. Bhagwandien, S. H. Muller, F. C. Verster, and M. B. van Herk. The computation of mr image distortions caused by tissue susceptibility using the boundary element method. *IEEE Trans Med Imaging*, **15**, 620–627. (1996).

[5] D. Yoder, E. Changchien, C. B. Paschal, and J. M. Fitzpatrick. Mri simulator with static field inhomogeneity. In *SPIE Proc. Medical Imaging: Image Processing*, volume 4684, pages 592–603, San Diego, CA, February 2002.

[6] J. P. Marques and R. Bowtell. Evaluation of a fourier based method for calculating susceptibility induced magnetic field perturbations. In *Proc. of ISMRM*, volume 10, page 216, (2003).

[7] M. Jenkinson, J. Wilson, and P. Jezzard. Perturbation calculation of B0 field for non-conducting materials. In *Proc. Int. Soc. of Magnetic Resonance in Medicine*, (2002).

[8] J. Schwinger, L. DeRaad Jr, K. A. Milton, and W. Y. Tsai. *Classical Electrodynamics*. Perseus Books, (1998).

[9] E. M. Haacke, R. W. Brown, M. R. Thompson, and R. Venkatesan. *Magnetic Resonance Imaging: Physical Principles and Sequence Design*. Wiley-Liss, (1999).

[10] P. Jezzard and R.S. Balaban. Correction for geometric distortion in echo planar images from B0 field variations. *Magnetic Resonance in Medicine*, **34**, 65–73. (1995).

[11] J. L. Wilson, M. Jenkinson, and P. Jezzard. Optimisation of static field homogeneity in human brain using diamagnetic passive shims. *Magn Reson Med*, **48**, 906–914. (2002).

[12] M. Jenkinson, P.R. Bannister, J.M. Brady, and S.M. Smith. Improved optimisation for the robust and accurate linear registration and motion correction of brain images. *NeuroImage*, **17**, 825–841. (2002).

[13] I S Gradstein and I H Ryshik. *Tables of Series, Products and Integrals*. , (1981).